JOURNAL OF SPACECRAFT AND ROCKETS
Vol. 40, No. 1, January–February 2003

Pseudodomain Fracture Analysis of Instrumented Analog Rocket Motors

F. C. Wong*
Defence Research and Development Canada—Valcartier, Val-Belair, Quebec G3J 1X5, Canada

An advanced stress analysis technique has been developed for evaluating propellant fracture in solid-rocket motors subjected to thermal cooling. When a strain-to-pseudostrain transformation is performed, it is shown that the time- and temperature-dependent relaxation of the solid propellant can be taken into account to yield a nonlinear elastic material model. This material model can be used in a finite element analysis of a solid-rocket motor grain to quantify the driving force for quasi-static crack propagation under a variety of thermal loads by using elastic–plastic fracture mechanics. The analysis technique was assessed by subjecting analog rocket motors instrumented with miniature bond-stress sensors to a sequence of quasi-isothermal temperatures. The data measured by the sensors allowed the stress predictions to be verified and the crack length and fracture resistance of the propellant to be deduced. It is hypothesized that compatibility must be maintained between the crack tip constraint conditions in the fracture specimen used to characterize a propellant and the crack tip constraint conditions in the structure being analyzed to use this analysis technique in a predictive manner.

Nomenclature

a	=	crack length, m
a_T	=	shift factor
C_1, C_2	=	Williams–Landel–Ferry parameters
E_i	=	Prony-series multiplier, MPa
E_o	=	equilibrium modulus, MPa
E_R	=	reference modulus, MPa
$E(t)$	=	relaxation modulus, MPa
e	=	engineering strain
J^e	=	pseudo-J integral, N · m/m^2 or Pa · m
M^j	=	slope of bond-line stress to crack length, MPa/mm
n	=	Ramberg–Osgood[12] exponent
T, T^j, T^k	=	temperature, °C
T_{ref}	=	reference temperature, °C
t	=	time, s
α	=	Ramberg–Osgood multiplier
α^e	=	pseudothermal expansion coefficient, 1/°C
α_{fac}	=	scaling factor, °C
α_{prop}	=	propellant thermal expansion coefficient, 1/°C
Δ	=	displacement, mm
Δ^e	=	pseudodisplacement, mm
ΔT	=	temperature change, °C
$\dot{\Delta} T$	=	temperature change rate, °C/s
$\Delta V/V$	=	average volume dilatation
ϵ	=	true strain
ϵ^e	=	pseudostrain
$\epsilon^e_{\text{thermal}}$	=	pseudothermal strain
ϵ_0	=	elastic strain limit
$\dot{\epsilon}$	=	strain rate, s^{-1}
σ	=	engineering stress, MPa
σ_B	=	sensor B bond stress, MPa
σ^j_{crack}	=	bond stress due to crack, MPa
σ^j_{damage}	=	bond stress due to damage, MPa
σ_T	=	true stress, MPa
σ_0	=	elastic stress limit, MPa
$\sigma^j_{(1)}, \sigma^k_{(1)}$	=	bond stress, MPa
$\sigma^j_{(2)}$	=	bond stress, MPa
τ_i	=	Prony-series time constant, s

Subscripts

d	=	deduced crack length
f	=	final crack length
(1)	=	first stepped-cooling cycle
(2)	=	second stepped-cooling cycle

Superscripts

j	=	temperature dwell in the cooling profile
k	=	final temperature in the cooling profile

Presented as Paper 2000-3324 at the AIAA/ASME/SAE/ASEE 36th Joint Propulsion Conference, Huntsville, AL, 17–19 July 2000; received 20 March 2002; revision received 24 July 2002; accepted for publication 3 September 2002.

*Defence Scientist, Precision Weapons Section, 2459 Boulevard Pie XI, North. Member AIAA.

Introduction

SOLID-ROCKET motors used by military forces are exposed to a variety of extreme conditions over time. Thermal cycling, on a microscopic scale, causes micromechanical damage in the form of oxidizer/polymer debonding, which gives rise to microcrack formation. On a macroscopic scale, when a sufficient number of microcracks coalesce, macroscopic cracks form. Macrocrack formation is undesirable because the macroscopic cracks may propagate unstably when exposed to extreme thermal cool-down conditions while the motors are in transit, or to ignition pressurization when the motor is fired. The increase in the burnable surface area leads to unexpected increases in chamber pressure. If the chamber pressure exceeds the burst pressure of the motor case, catastrophic failure occurs. It is imperative, therefore, that a structural analysis technique be available to predict the potential for thermally induced fracture in solid propellants as part of the procedure used to analyze solid-rocket motors.

Composite solid propellants are thermononlinear viscoelastic materials. Past efforts to quantify the driving forces at the crack tip treated a propellant as if it were a viscoelastic brittle material, assuming that fracture was controlled by small-scale yielding and, therefore, could be quantified by the stress intensity factor K. For example, Knauss[1] studied crack propagation in an unfilled carboxyl-terminated hydrocarbon rubber. Crack tip velocities were measured in edge notched specimens at different temperatures. A master curve based on linear elastic fracture mechanics, that is, K_I, was created to distinguish between regions of stable and unstable crack growth. In another study, Bennett et al.[2] derived equations to calculate the failure strain that are based on time, relaxation modulus and the time-dependent Griffith formulation by using cohesive fracture energy, that is, γ_c. Francis et al.[3–5] conducted several studies by using

epoxy, Solithane 113, and PBAN propellant in a biaxial and a plane stress analog motor configuration. Like Knauss,[1] they based driving force calculations on stress intensity. They found that a one-to-one correspondence existed between the viscoelastic K_I and the crack velocity.

The previous studies had some success in quantifying the energy at the crack tip, but the methods were limited to those conditions where the material tended to behave in a brittle manner. The development of elastic–plastic fracture mechanics provided a new way to account for crack tip plastic zones in ductile materials. Bencher et al.[6] applied elastic–plastic fracture mechanics as defined by the J integral to characterize the fracture resistance of an inert solid propellant. The time–temperature dependency of the model propellant was dealt with by employing Schapery's pseudostrain concept.[7] Although their work was limited to the analysis of data from middle-tension test specimens, the idea of combining the pseudostrain concept and elastic–plastic fracture mechanics offered a computationally attractive scheme to predict crack propagation in solid-rocket motor geometries.

The present study discusses the development of a numerical and experimental stress analysis technique for evaluating propellant fracture in solid-rocket motors subjected to monotonic thermal cooldown loading. The pseudostrain technique developed by Schapery[7] is applied to a typical composite propellant widely used in solid-rocket motors to change its time and temperature-dependent behavior to resemble that of a nonlinear elastic, or what can be considered an equivalent elastic–plastic material. With this approach, existing elastic–plastic fracture theories for stationary cracks and commercial finite element programs can be used for propellant fracture analysis. The dependency on linear elastic fracture mechanics and the cumbersome treatment of the viscoelastic problem can both be avoided as well. To assess the applicability of this proposed method, the numerical stress and fracture results are compared with experimental data obtained from instrumented analog solid-rocket motors.

Pseudoproperties Determination

Schapery[7,8] proposed the use of pseudostrains as a method of transforming the viscoelastic behavior of a polymer into the time-independent behavior that is typically seen in metals. This method is based on the assumption that the time-dependent modulus of the viscoelastic material is separable from the material strain. If this transformation is valid, then the fracture analysis of a viscoelastic propellant can be greatly simplified because the problem can be reduced to a fracture analysis of an elastic–plastic or nonlinear elastic material. Interested readers may refer to Refs. 9 and 10 for a more detailed discussion on the limitations of this theory.

The procedure that is used herein to transform propellant characterization data to an elastic–plastic representation comprises four steps. They are as follows: 1) Calculate the true stress and true strain. 2) Characterize the stress relaxation behavior. 3) Calculate the pseudostrain. 4) Fit the data to the Ramberg–Osgood[11] constitutive equation.

Finite element programs are based on work conjugate stress–strain pairs. For the ANSYS finite element program used in this study, the work conjugate pair is based on true stress and true strain. The first step in the transformation process is to convert the engineering stress–strain data from uniaxial tensile tests to true stress–strain values by using

$$\epsilon = \ln(1 + e) \tag{1}$$

$$\sigma_T = \sigma(1 + e)/[1 + (\Delta V/V)] \tag{2}$$

For viscoelastic materials, the stress relaxation behavior is represented by a Prony series with a shift factor that is based on the Williams–Landel–Ferry (WLF) relationship (see Ref. 12)

$$\int_0^t E(t - z)\,\mathrm{d}z = \int_0^t E_o + \sum_{i=1}^{m} E_i \exp\left(-\frac{z}{a_T \tau_i}\right)\mathrm{d}z \tag{3}$$

$$\log a_T = -\frac{C_1(T - T_{\text{ref}})}{C_2 + (T - T_{\text{ref}})} \tag{4}$$

where E_o, E_i, and τ_i are the Prony coefficients and a_T is the temperature shift factor.

Schapery defined pseudostrain as the strain rate multiplied by the integral of the time-dependent tensile modulus

$$\epsilon^e = \dot{\epsilon} \int_0^t E(t - z)\,\mathrm{d}z \tag{5}$$

where $E(t - z)$ is the relaxation modulus. Substituting Eq. (3) into Eq. (5) and integrating gives

$$\epsilon^e = \frac{\dot{\epsilon}}{E_R}\left\{E_o t + \sum_{i=1}^{m} a_T E_i \tau_i \left[1 - \exp\left(-\frac{t}{a_T \tau_i}\right)\right]\right\} \tag{6}$$

where E_R is set equal to the glassy modulus. Equation (6) indicates that if the material is linear viscoelastic, the true stress/true strain data will form a single nonlinear elastic curve.

The Ramberg–Osgood constitutive equation[11] was used to represent the time- and temperature-independent pseudostrain vs true stress behavior

$$\epsilon/\epsilon_0 = \sigma/\sigma_0 + \alpha(\sigma/\sigma_0)^n \tag{7}$$

where ϵ_0 and σ_0 are the reference values and a and n are the Ramberg–Osgood parameters.[11] It was advantageous to adopt this formulation because of its extensive use in elastic–plastic fracture mechanics.[13,14]

To prove that this reduction method is applicable to composite propellants, a hydroxyl-terminated polybutadiene/ammonium perchlorate (HTPB/AP) propellant, in the shape of a JANNAF Class C dogbone specimen,[15] was tested under uniaxial tension over a temperature range from +50 to −50°C and at crosshead rates of 5, 50, and 500 mm/min. The relaxation data were measured by dynamic mechanical analysis.[16] The results of applying Eqs. (1–7) to the uniaxial test results are shown in Figs. 1 and 2.

Figure 1 shows the measured true stress vs true strain behavior for tests at 50 mm/min. The Prony-series coefficients used in Eq. (6) are given in Table 1. The ability of Eq. (6) to transform the disparate true stress vs true strain curves (Fig. 1) into a monotonically increasing set of true stress vs pseudostrain data is shown in Fig. 2. Similar results were obtained for the 5- and 500-mm/min data. Though the −50, −45, −30, +22, and +50°C data in Fig. 2 have not been perfectly transformed to form a single curve, the data set can be parameterized by using the Ramberg–Osgood[11] equation to permit its use in an elastic–plastic analysis.

The Ramberg–Osgood[11] parameters were found to be $\alpha = 0.0671$, $n = 2.565$, $\epsilon_0 = 0.0011$, and $\sigma_0 = 500$ kPa by fitting Eq. (7) to the data from all crosshead rates (see Fig. 3) with the TableCurve2D program.[17] The correspondence between the regenerated results (solid predicted lines) and the original data in Fig. 1 suggests that this method can be used to transform the viscoelastic propellant

Table 1 Prony-series coefficients[a−e]

G_i, MPa	τ_i, s
44.0	2.16×10^{-8}
21.9	1.50×10^{-7}
13.5	1.04×10^{-6}
8.89	7.23×10^{-6}
7.41	5.02×10^{-5}
5.22	3.49×10^{-4}
3.29	2.42×10^{-3}
1.87	1.68×10^{-2}
1.08	1.17×10^{-1}
0.66	8.09×10^{-1}
0.41	5.62×10^{0}
0.31	3.90×10^{1}
0.21	2.71×10^{2}
0.10	1.88×10^{3}

[a]Equilibrium modulus $G_e = 1.30$ MPa.
[b]Tensile modulus obtained by assuming Poisson ratio equal to 0.5.
[c]$C_1 = 6.98$.
[d]$C_2 = 190.7$.
[e]T_{ref} (Kelvin) = 293.8.

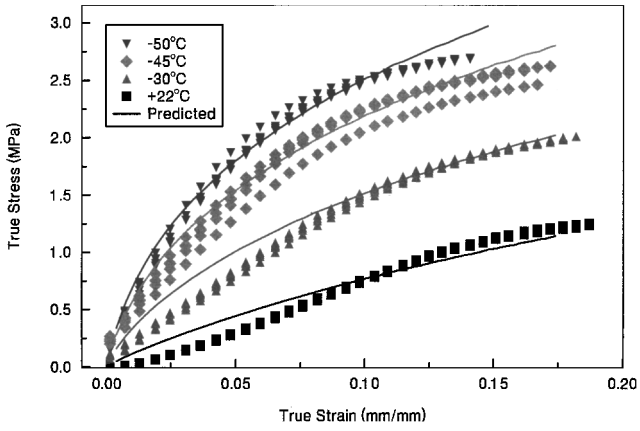

Fig. 1 True stress vs true strain data of an HTPB/AP propellant tested at a 50-mm/min displacement rate.

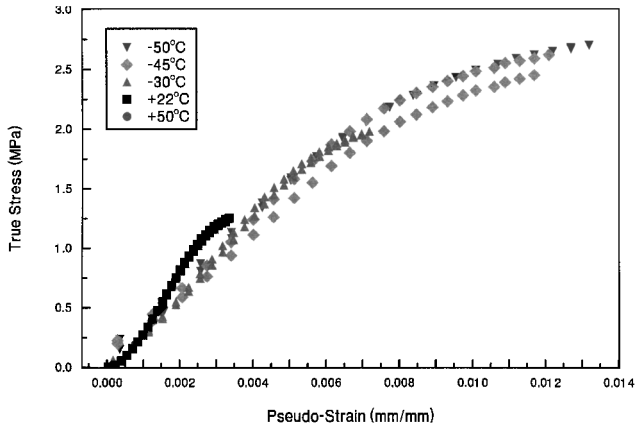

Fig. 2 True stress vs pseudostrain data of an HTPB/AP propellant tested at a 50-mm/min displacement rate.

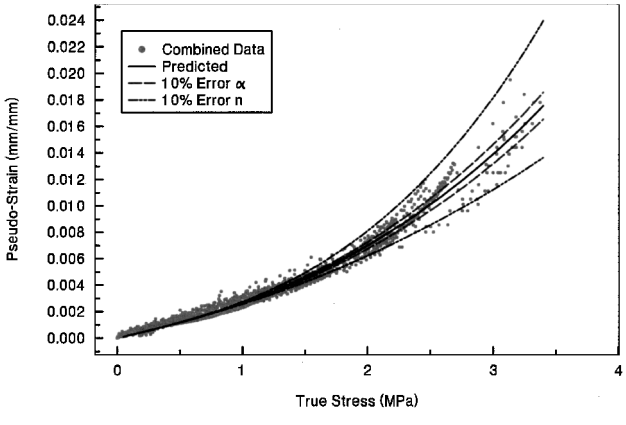

Fig. 3 Ramberg–Osgood[11] predictions of pseudostrain vs true stress data with 10% error in the α or n values.

properties to an equivalent elastic–plastic or nonlinear elastic material. The effect of data scatter on the Ramberg–Osgood[11] parameters and the calculated stress results will be discussed later in the Error Analysis section.

Finite Element Analysis

Model and Solution Method

The cross section of an instrumented analog motor (IAM) is schematically shown in Fig. 4. The IAM comprises a composite casing, two bond-stress sensors mounted on platforms, and propellant cast with a stress raiser geometry. A bond-stress sensor with its bridge completion circuit and mounting platform is shown in Fig. 5. The geometry of the stress raiser (Fig. 6) was designed to maximize

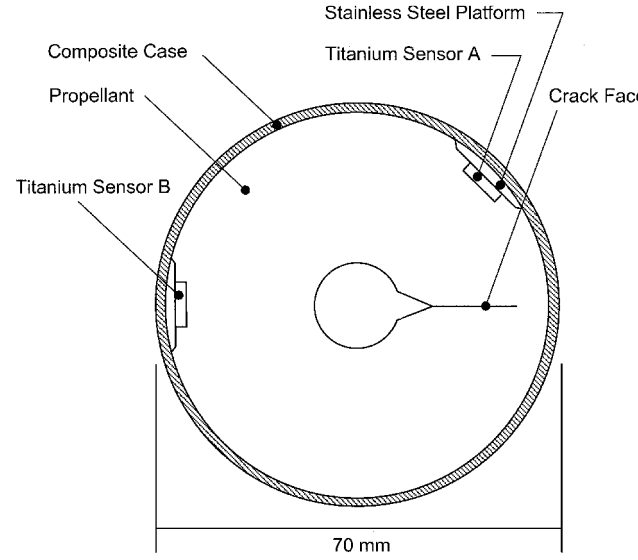

Fig. 4 Schematic diagram of an instrumented analog motor.

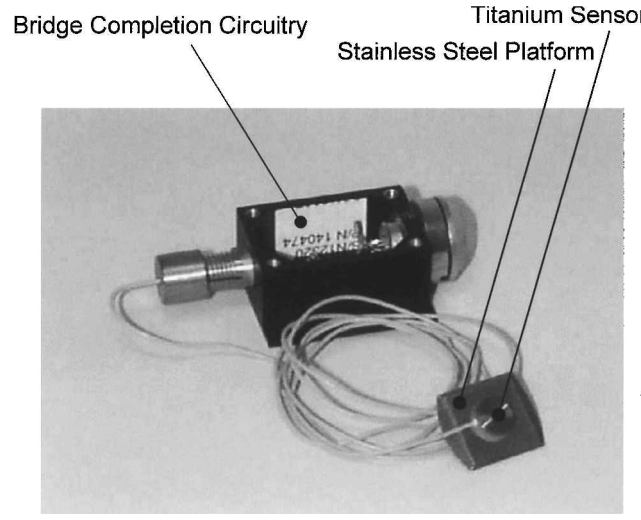

Fig. 5 Bond-stress sensor mounted on a platform and the bridge completion circuitry.

the driving force at the crack tip and to orient the crack propagation so that two strategically located bond-stress sensors could adequately measure the changes in the far-field stresses.[10] Sensor A is positioned at an angle $\varphi = 45$ deg to the crack face, whereas sensor B is positioned at $\varphi = 180$ deg. These positions were selected by examining the radial bondline stress results from finite element analyses. The stresses at these two positions gave the greatest stress magnitude difference (sensor B stress − sensor A stress) and the highest stress ratio (sensor B stress/sensor A stress) as a function of crack length. The sensors provide a direct means of verifying the stress predictions and an indirect method for evaluating fracture behavior of the propellant.

A finite element model of the IAM was constructed with the PLANE82 structural elements in plane strain mode in ANSYS.[18] This element has eight nodes with two degrees of freedom at each node. The nodes and elements around the crack tip were defined by using the KSCON command. This ANSYS command places nodes at quarter-point locations. Free meshing was used for all areas, with the exception of the sensors, where mapped meshing was specified.

The ANSYS frontal solver, coupled with a full Newton–Raphson incremental solution, was employed to resolve the nonlinear elastic problem. The frontal solution procedure is based on the work of Irons[19] and Melosh and Bamford,[20] where elements are processed to make efficient use of the available computer resources. The method

Table 2 Finite element model material parameters

Parameter	Value
Composite case	
E_{case}	974.9 GPa
ν_{case}	0.33
α_{case}	0/°C
SS 304 sensor platform[a]	
E_{plat}	193.0 GPa
ν_{plat}	0.25
α_{plat}	17.3×10^{-6}/°C
Titanium stress sensor[a]	
E_{sensor}	114.5 GPa
ν_{sensor}	0.34
α_{sensor}	9.54×10^{-6}/°C
Propellant	
E_{prop}	Variable
ν_{prop}	0.495
α_{prop}	8.5×10^{-5}/°C

[a]Here, α is set to zero for analyses in the pseudodomain and a stress-free temperature of 60°C is used. A value of $\nu_{prop} = 0.495$ is used to account for the small amount of volume dilatation that occurs during tensile straining.

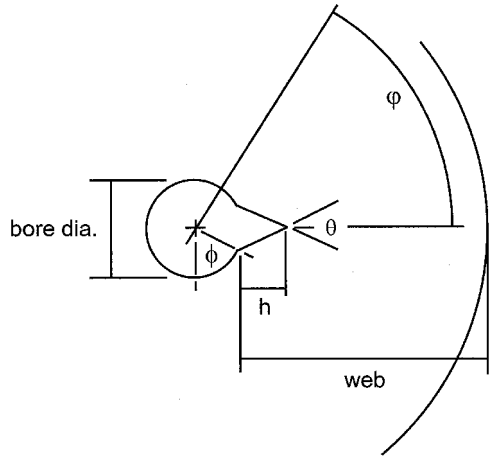

Fig. 6 Bore geometry employed in the instrumented analog motor: bore diameter = 14.7 mm, web = 25.7 mm, h = 5.4 mm, ϕ = 71.49 deg, and θ = 49 deg.

for treating a nonlinear elastic material follows procedures already established for resolving rate-independent plasticity problems.[21] A stress-free temperature of 60°C, which corresponds to the casting temperature, was used in the stress analysis. The J integral was calculated by using a virtual crack extension method that is based on stiffness derivatives for six different contours located from one to six element lengths beyond the first row of elements around the crack tip. Results were averaged afterward to obtain the value for the pseudo-J integral J^e. In general, the values of J^e were within 2% of each other. For additional information on the procedure used to calculate J, see Ref. 14 or 22. Stress and J^e solutions were generated for a series of temperature loads and crack lengths.

Material Properties

Table 2 gives a summary of the properties used in the finite element model. The true stress versus pseudostrain propellant behavior as defined by the best-fit Ramberg–Osgood[11] parameters was modeled in ANSYS as a multilinear isotropic hardening material.[18] All other materials were assumed to exhibit linear elastic behavior.

Because the analyses were carried out in the pseudodomain, it was important to ensure that all strains were properly scaled. The propellant thermal expansion coefficient in Table 2 was scaled to produce thermal strains consistent with the strain measure in the material model. The scaling factor can be derived by substituting the definition of thermal strain, $\epsilon = \alpha \Delta T$, into Eq. (6), to give

$$\epsilon^e_{\text{thermal}} = \frac{\alpha_{\text{prop}} \dot{\Delta T}}{E_R} \left\{ E_o \Delta t + \sum_{i=1}^{m} a_T E_i \tau_i \left[1 - \exp\left(-\frac{\Delta t}{a_T \tau_i} \right) \right] \right\} \tag{8}$$

where E_o, E_i, and τ_i are the Prony coefficients and a_T is the WLF shift factor. The scaling factor α_{fac} is defined as

$$\alpha_{\text{fac}} = \frac{\dot{\Delta T}}{E_R} \left\{ E_o \Delta t + \sum_{i=1}^{m} a_T E_i \tau_i \left[1 - \exp\left(-\frac{\Delta t}{a_T \tau_i} \right) \right] \right\} \tag{9}$$

ANSYS requires pseudothermal strains to be defined in the following form

$$\epsilon^e_{\text{thermal}} = \alpha^e \Delta T \tag{10}$$

Combining Eqs. (8) and (9) with Eq. (10) gives

$$\alpha^e = \alpha_{\text{prop}} \alpha_{\text{fac}} / \dot{\Delta T} \tag{11}$$

The effective expansion coefficient for a linear elastic, or time-independent, material is derived by recognizing that a linear elastic material can be modeled by setting $\tau_i \gg 1$. Because

$$\sum E_i = E$$

where E is the linear elastic modulus, the sum implies that $E_o = 0$. With $\tau_i \gg 1$ and $E_o = 0$, α_{fac} for a linear elastic material in a pseudothermal strain analysis equals zero.

Given the dependency of the scaling factor α_{fac} on the rate of temperature change $\dot{\Delta T}$ and the time increment at a particular temperature Δt, the α_{fac} had to be calculated for the planned sequential quasi-isothermal cooling or stepped-cooling test. The temperature vs time profiles for the IAM could have been calculated by using finite element thermal analysis. For the case considered herein, it was measured directly from an instrumented IAM that was subjected to a thermal profile that consisted of a heat-up cycle followed by stepped cooling. The heat-up cycle raised the temperature of the IAM to +65°C in 12 h and cooled it back to room temperature in the same amount of time, followed by a 3-h dwell. The heat-up cycling was immediately followed by decreasing the conditioning chamber temperature to −10°C for 6 h with subsequent 5°C step decreases over a 36-h period. The temperature dwell at each 5°C decrease was maintained for 6 h.

The α_{fac} was determined by using an average temperature rate over a time increment of 120 min. The time increment corresponds to the thermal time constant of the IAM. Table 3 gives the time, temperature, and $\alpha_{\text{fac}}/\dot{\Delta T}$ used in the finite element analyses.

Numerical Results

Figure 7 shows the predicted pseudo-J driving forces J^e as a function of the crack length for several thermal loads. The common units of J in N · m/m^2 have been altered to the equivalent units Pa · m in this paper for typographical reasons. A nearly exponential trend of increasing J^e with decreasing temperature is shown. The absolute variation with crack length increases as temperature

Table 3 Pseudothermal expansion coefficient multipliers for a stepped-cooling profile

$\sum t$, days	Δt, s	T, °C	$\alpha_{\text{fac}}/\dot{\Delta T}$
0	——	60	——
0.2604	22,499	50	0.0118
0.5215	22,559	20	0.0118
N/A	N/A	0	≈0.0120[a]
0.6604	12,001	−10	0.0126
0.8514	16,502	−15	0.0137
1.0910	20,701	−20	0.0142
1.3410	21,600	−25	0.0149
1.5993	22,317	−30	0.0159
1.8320	20,105	−35	0.0174
2.0889	22,196	−40	0.0187

[a]Estimated value.

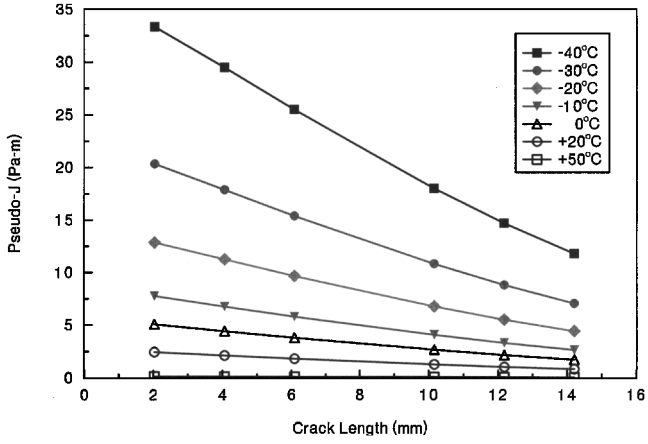

Fig. 7 Predicted pseudo-J driving forces in an instrumented analog motor as a function of crack length for several temperatures.

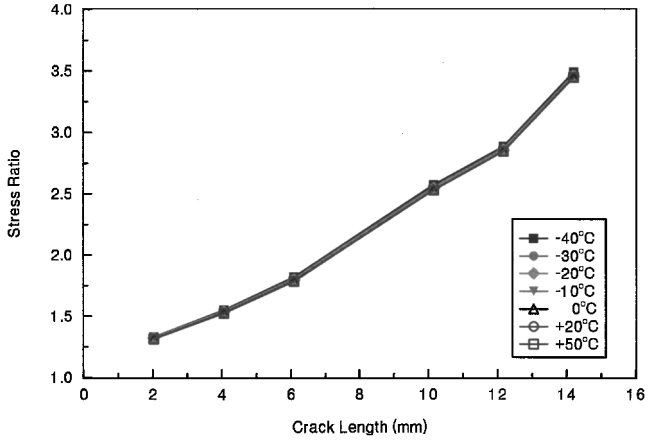

Fig. 8 Ratio of the predicted sensor B to sensor A stresses in an instrumented analog motor as a function of crack length for several temperatures.

decreases, although the relative change based on the maximum J^e is approximately 63%. For example, at −40°C, the absolute change in J^e from 2 to 14 mm is 21 Pa · m with a maximum value for J^e of 33 Pa · m. At −10°C, the change is 5 Pa · m with a maximum value of 7.5 Pa · m. These results suggest that decreasing the temperature will dramatically increase the driving force that causes crack initiation. Crack propagation, however, will dissipate some of this energy.

Figure 8 shows the ratio of the radial stress at sensor B to that at sensor A as a function of crack length. An increase in this ratio is predicted for both decreasing temperature and increasing crack length. In general, the stress ratio can be used to determine crack length but not at a specific temperature because the stress ratio magnitudes at different temperatures are similar.

Figures 9 and 10 illustrate the absolute sensor readings (radial stress) for several temperatures at locations A and B, respectively, as a function of crack length. The results show that the sensor B predictions are always higher than the sensor A predictions. Also, the sensor A results decrease more rapidly with increasing crack length than those for sensor B. In Fig. 10, the sensor stresses for each temperature differ (by about 100 kPa) even as the crack length increases. In Fig. 9, the sensor stresses differ at small cracks sizes (by approximately 50 kPa), but this difference decreases to about 10 kPa for the longer crack lengths.

From these results, one could estimate the crack propagation temperature and the crack length from either the sensor A or B readings. Having two sensors in the IAM allows the consistency of the stress readings to be checked, and it provides a measure of redundancy in the event that one sensor malfunctions. Based on the stress predictions for sensor A, the sensors used in any experiment need to be accurate to at least ±10 kPa or better. Inspection of the sensor B results showed that its accuracy is on the order of ±35 kPa or better.

Table 4 Error induced by uncertainty in the exponent n from Ramberg–Osgood[11] [a]

Parameter	Avgerage	% difference low	% difference high
J^e, Pa · m	6.263	0.1	−0.1
Sensor A, MPa	1.208	0.6	−0.6
Sensor B, MPa	1.278	0.7	−0.7
Stress ratio B/A	1.058	0.0	0.0

[a]Temperature set at −40°C with crack length = 2.5 mm.

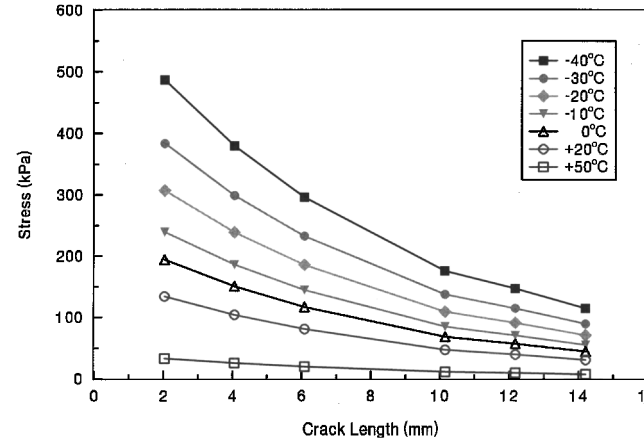

Fig. 9 Radial stress predictions for sensor A in an instrumented analog motor as a function of crack length for several temperatures.

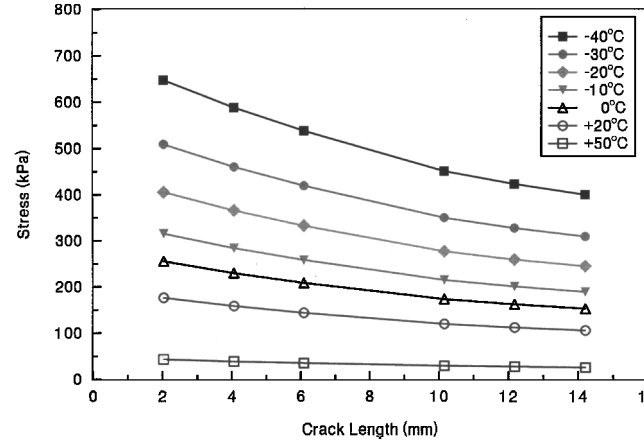

Fig. 10 Radial stress predictions for sensor B in an instrumented analog motor as a function of crack length for several temperatures.

Error Analysis

The propellant stress–strain properties used herein are based on the best-fit Ramberg–Osgood[11] model [Eq. (7)]. As with any curve fitting, there is some uncertainty associated with the scatter in the raw data. Recall that the scatter in the data set is caused by the transformation of stress–strain data originally measured at several temperatures and strain rates. To assess the effects that this inherent error could have on the numerical results, two analyses were conducted that vary $n = 2.565$ to values that corresponded to an error of ±10%. The sensitivity of α was not studied because its influence is not as significant. Figure 3 shows that the 10% error α curves are well inside the 10% error n curves. The results of these calculations for a single temperature and crack length are tabulated in Table 4. As can be seen in Table 4, varying n has little or no effect on the results. This result is obtained because the calculated propellant stresses are well below 2.5 MPa, where data scatter becomes large.

Experimental Verification

Two instrumented IAMs, referred to as T212 and T214 herein, having the geometry defined by Figs. 4 and 6 and fabricated with the materials listed in Table 2, were subjected to a stepped-cooling

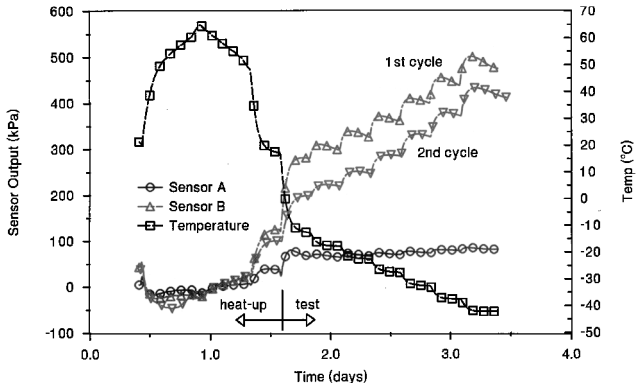

Fig. 11 Bond-stress and temperature data measured during first and second stepped-cooling cycles.

profile in a microprocessor-controlled conditioning chamber. The IAMs were 600 mm long to ensure that plane strain conditions existed at the midpoint of the analog motor. Each IAM was instrumented with two miniature titanium bond-stress sensors and two type-T needle thermocouples. The sensors measured 8 mm in diameter by 2 mm thick. Bond-stress sensors of this type were used with success in previous programs that measured stresses in solid-rocket motors.[23–27] Discussion of sensor calibration and installation is found in the report by Wong and Giasson.[10] Generally, the sensors had an accuracy of ±29 kPa or better.[28] The sensors were powered by constant current amplifiers set to 4 mA. A data acquisition system comprising a five and one-half digit voltmeter and a 20-channel relay multiplexer with thermocouple compensation were used to record sensor voltage output and thermocouple readings at 5-min intervals.

Thermal Cycling Results

For brevity, only the T214 stepped-cooling results are discussed in detail. The T212 results are shown elsewhere for completeness.

The resulting propellant thermal profile for stepped-cooling is shown in Fig. 11. As discussed earlier, the heat-up portion of the profile was used to bring the IAM to the propellant's stress-free state so that sensor offsets could be calculated and subtracted from the data. The cool-down portion was designed to hold the IAM at various temperatures so that quasi-static propellant fracture could take place under quasi-isothermal conditions. The IAM was exposed to the same thermal profile twice. The first cycling caused the crack to propagate at each dwell temperature. The second allowed additional data to be taken under assumed constant crack length conditions. This assumption is reasonable because the longer crack length in the IAM during the second cycling means the driving forces are lower at every dwell temperature. Crack propagation only occurs if the IAM is subjected to a temperature colder than the coldest temperature used in the first cycling.

The bond-stress and propellant temperature data for T214, for the two thermal cycles, are shown in Fig. 11. Both sensors measure compressive stresses as the IAM is heated to 65°C. As the temperature is reduced to 50°C, a small asymmetry is seen in the sensor data. This asymmetry was caused by the hysteresis behavior of the sensors. In the stepped-cooling segments, sensor A stresses started off at 76.0 kPa, at −10°C, and remained nearly constant throughout the sequence. The final stress reading at −40°C was 84.3 kPa. For sensor B, the bond-stresses increased by 30 kPa with each 5°C drop in temperature. Stress relaxation is seen at each step. At −40°C, the sensor B stresses reached 493 kPa and relaxed to 478 kPa in 6 h. The experimental B/A stress ratio increased with decreasing temperature in the cool-down portion of the cycle (Fig. 12). The data spikes in the heat-up portion of the cycle were caused by nonequilibrium thermal conditions experienced by the sensors.

When T214 was cycled again by using the same thermal profile, the sensor response changed slightly. The sensor A stresses in the stepped-cooling segments began lower at 33.1 kPa at −10°C and rose to 78.7 kPa at −40°C (not shown in Fig. 11). Sensor B also began lower at 192 kPa and finished at 433 kPa. Relaxation behavior can again be seen. The B/A stress ratio remained fairly constant at about 5.4 (not shown in Fig. 12).

Table 5 Comparison of predicted and measured bond-stress results for T214 stepped cooling[a]

	Finite element		Experimental	
Temperature, °C	Sensor A, kPa	Sensor B, kPa	Sensor A, kPa	Sensor B, kPa
−10	70.4	201	33.1	192
−20	90.7	259	46.2	249
−30	114	327	64.1	329
−40	147	423	78.7	433

[a]Crack 12 mm long, finite element error ±0.7%, sensor A error ±11 kPa, and sensor B error ±29 kPa.

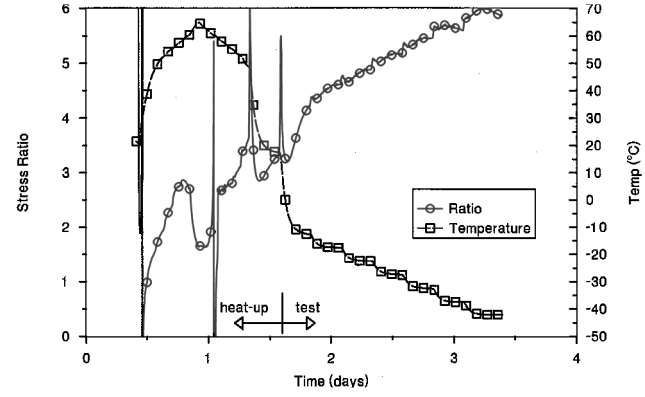

Fig. 12 Ratio of measured sensor B to sensor A stress data and temperature data measured during first stepped-cooling cycles.

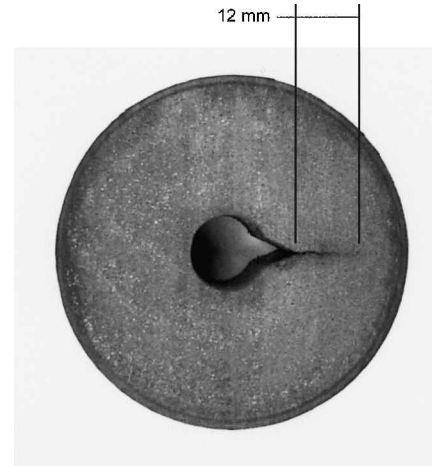

Fig. 13 Measurement of the final crack length in an uninstrumented analog motor.

To obtain additional data, uninstrumented analog motors were cycled along with the IAMs in the stepped-cooling tests. They were subsequently cut along several longitudinal stations to allow direct measurement of the crack length. A typical crack was found to propagate in a radial direction away from the stress-raiser peak (Fig. 13). The final crack lengths for the step-cooled IAMs measured roughly 12 mm long.

Sensor B and Deduced Fracture Behavior

In comparison with the predicted B/A stress results (Fig. 8), the experimental B/A stress ratio data for the stepped-cooling sequence exhibited the same trend for a growing crack, but the absolute values did not correspond. Table 5 shows a comparison of the measured and predicted bond stresses for a crack length of 12 mm.

The sensor A data were on average 48% lower than the finite element predictions, whereas the sensor B differences varied between −5 and +2%. It was determined on subsequent investigation that sensor A had become partially debonded at the lower temperatures because of radial and shear stresses present on the sensing diaphragm. As a result, sensor A indicated lower than expected stress

Table 6 Estimates of crack length from sensor B[a] measurements for T214 stepped cooling

Measured data			Derived results				
Temperature, °C	Sensor $B_{(1)}$,[b] kPa	Sensor $B_{(2)}$,[c] kPa	Temperature, °C	σ^j_{dam}, kPa	σ^j_{crack}, kPa	a^j_d,[d] mm	J^e at j,[e] Pa·m
−10	278	192	−10	27	59	6.75 ± 0.01	5.51 ± 0.01
−20	337	249	−20	35	53	8.63 ± 0.33	7.83 ± 0.23
−30	408	329	−30	46	33	9.67 ± 0.25	11.3 ± 0.3
−40	493	433	−40	60	0	12.1 ± 0.6	14.8 ± 1.0

[a]Sensor B error is ±29 kPa.
[b]Stress at sensor B during the first thermal cycle.
[c]Stress during the second thermal cycle.
[d]Deduced crack length.
[e]Deduced pseudo-propellant fracture resistance at temperature index j.

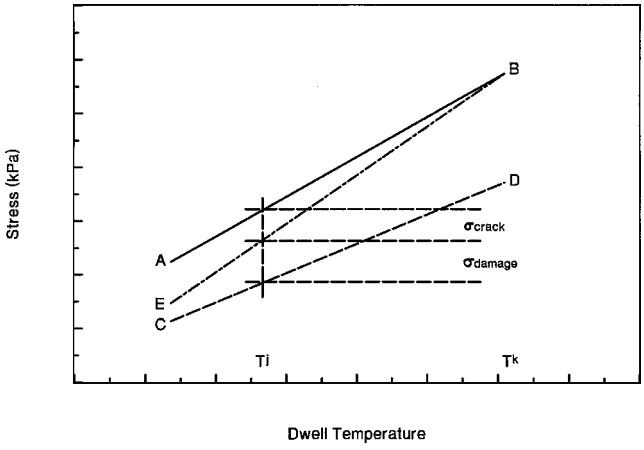

Fig. 14 Schematic representation of sensor B data after the first and second stepped-cooling cycles.

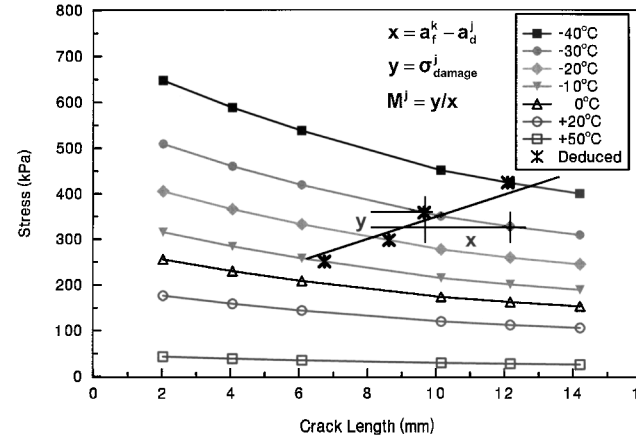

Fig. 15 Deduced crack lengths at several temperatures based on measured sensor B data for instrumented analog motor T214.

readings. The sensor B readings showed that the pseudostrain vs true stress transformation approach gave reasonable stress predictions.

If the crack had propagated during the first application of the thermal cooling profile and remained at a constant length during the second application of the cooling cycle, the sensor B data could be used to deduce the crack length at each temperature dwell by employing the following procedure.

Figure 14 shows a schematic representation of the stepped-cooling sensor B data from Fig. 11 in relation to the dwell temperature T^j and the final dwell temperature T^k. Line AB represents the sensor data measured during the first cooling profile. These stresses are a function of a changing crack length and microstructural propellant damage. Line CD represents the sensor data measured during the second cooling profile. These stresses are a function of an assumed constant crack length and microstructural propellant damage. The damage is in the form of microscopic debonding that occurs between the ammonium perchlorate particles and the polybutadiene binder. The debonds effectively lower the macroscopic propellant modulus by nullifying the stiffness properties of the hard perchlorate particles.[29] This type of damage is commonly seen in solid propellants and composite materials when they are tested under a constant magnitude cyclic load.[30] The observed maximum strain at each peak stress is increased because microstructural damage accumulates with each cycle. In the IAM, the microstructural damage manifests itself as a reduction in the propellant modulus and, therefore, lower sensor stresses.

To separate the stress reduction caused by crack extension σ^j_{crack} from the stress reduction caused by microstructural damage σ^j_{damage}, it is hypothesized that σ^j_{damage} at any dwell temperature T^j is proportional to the damage observed during the final dwell temperature T^k on the second stepped-cooling cycle, or

$$\sigma^j_{damage} = \left(\sigma^k_{(1)} / \sigma^k_{(2)}\right) \cdot \sigma^j_{(2)} \tag{12}$$

where σ^j_{damage} is the damage measure, $\sigma^j_{(1)}$ is the stress during first thermal cycle, and $\sigma^j_{(2)}$ is the stress during the second thermal cycle. The stresses associated with crack length can then be calculated by

$$\sigma^j_{crack} = \sigma^j_{(1)} - \left(\sigma^j_{damage} + \sigma^j_{(2)}\right) \tag{13}$$

where the sum of σ^j_{damage} and $\sigma^j_{(2)}$ is shown schematically as line EB in Fig. 14.

Once σ^j_{crack} is known at each dwell temperature T^j the crack extension that took place during the first stepped-cooling cycle a^j_d can be calculated using

$$\sigma^j_{crack} = M^j\left(a^k_f - a^j_d\right) \tag{14}$$

where M^j is the piecewise slope of the finite element calculated sensor B stress vs crack length response at temperature index j (Fig. 10) and a^k_f is the final crack length at the final temperature index k during the first stepped-cooling cycle.

Having measured a final crack length a^k_f of 12 mm in IAM T214, the crack lengths at the other dwell temperatures a^j_d were deduced by using Eq. (14). The calculation of crack length (indicated by the deduced data points) in relation to the sensor B predictions (indicated by the −40, −30°C, etc., data points) is shown schematically in Fig. 15 for IAM T214 where $y = \sigma^j_{crack}$ and $x = a^k_f - a^j_d$. Thus, by only knowing the final crack length and the sensor B stress readings, it is possible to deduce the crack length at each dwell temperature. Once the sensor B stress to crack length ($\sigma_B - a$) correlation is known, the relationship between pseudo-J integral and crack length ($J^e - a$) and the relationship between sensor A stress and crack length ($\sigma_A - a$) is also known because the finite element results give the correlation between all four parameters σ_A, σ_B, J^e, and a.

To verify the consistency of the analysis, the deduced crack lengths at the corresponding temperatures were mapped onto the sensor A finite element predictions (see Fig. 16). The trend of the predicted sensor A stresses with crack length, or, alternatively, temperature or time, matches the experimental data in Fig. 11 well; that is, the sensor A stresses remained fairly constant at each dwell temperature or time step. As mentioned before, partial debonding of the propellant from the sensor diaphragm reduced the experimental sensor readings from the expected predicted levels.

Table 6 shows the numerical results for the T214 fracture resistance calculations that were obtained using Eqs. (12–14). The

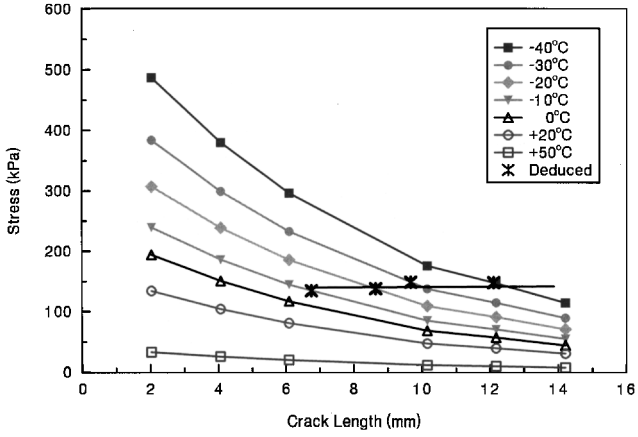

Fig. 16 Deduced sensor A stresses as a function of crack length for several temperatures.

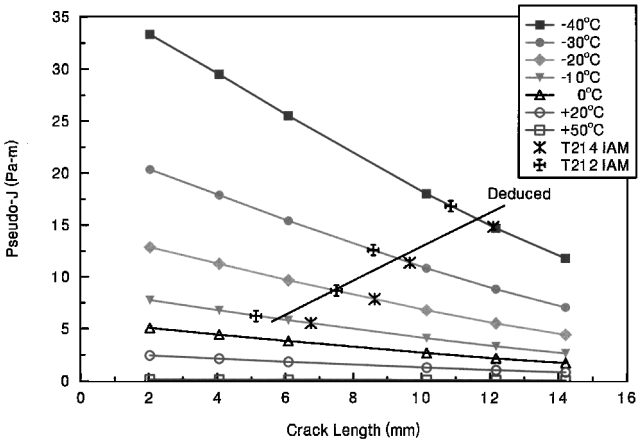

Fig. 17 Deduced pseudofracture resistance of the HTPB/AP propellant used in the instrumented analog motors.

numerical error bands are based on the accuracy of the sensor B readings. Figure 17 shows graphically the deduced crack lengths for T212 and T214 data. The average fracture resistance of the propellant can be estimated by the T212 and T214 data points.

To use the analysis technique developed here in a predictive manner, it is hypothesized that the crack tip constraint conditions in the test specimen used to characterize fracture resistance must be similar to the crack tip constraint conditions in the finite element model of the structure.[31] The constraint condition is defined as the ratio of the hydrostatic stress to the von Mises stress (see Refs. 32 and 33). The similitude of constraint conditions would permit the experimental fracture resistance data to be plotted onto finite element results, like in Fig. 17, to predict quasi-static crack growth. The validity of this approach and the methods to calculate the pseudo-J integral from fracture resistance testing are subjects of future research.

Conclusions

An advanced stress analysis technique has been developed to evaluate propellant fracture in solid-rocket motors subjected to thermal cool-down loading. The results show that the time- and temperature-based relaxation of the propellant can be taken into account through a pseudostrain representation to yield a nonlinear elastic material model. Finite element analyses of an instrumented analog motor were performed to quantify the quasi-static driving force for crack propagation under a variety of thermal loads. Tests were carried out on instrumented analog motors by subjecting them to a sequence of quasi-isothermal temperatures. A comparison between the measured sensor data and the corresponding finite element predictions shows that the stress analyses produced accurate results. The sensor data allowed the crack length and fracture resistance of the propellant to be deduced by assuming that the stress difference between successive thermal cycles is caused by crack propagation and bulk propellant damage effects. To use this analysis technique in a predictive manner, it is hypothesized that compatibility must be maintained between the crack tip constraint conditions in the fracture test specimen used to characterize the propellant and the crack tip constraint conditions in the structure being analyzed.

Acknowledgments

The author would like to thank the Defence R&D Canada—Valcartier management for their support in this work and David Erickson, Research Assistant, for his help in carrying out some of the ANSYS calculations. The supply of bond-stress sensors used in this study by H. J. Buswell, Defence Science and Technology Laboratory (Malvern), Worcestershire, England, U.K., is gratefully acknowledged. The many constructive comments given by the reviewers and Associate Editor are also appreciated.

References

[1]Knauss, W. G., "Stable and Unstable Crack Growth in Viscoelastic Media," *Society of Rheology Transactions*, Vol. 13, No. 3, 1969, pp. 292–313.

[2]Bennett, S. J., Anderson, G. P., and Williams, M. L., "The Time Dependence of Surface Energy in Cohesive Fracture," *Journal of Applied Polymer Science*, Vol. 14, No. 3, 1970, pp. 735–745.

[3]Francis, E. C., Lindsey, G. H., and Parmerter, R. R., "Pressurized Crack Behavior in Two-Dimensional Rocket Motor Geometries," *Journal of Spacecraft and Rockets*, Vol. 9, No. 6, 1972, pp. 415–419.

[4]Francis, E. C., Carlton, C. H., and Lindsey, G. H., "Viscoelastic Fracture of Solid Propellants in Pressurized Loading Conditions," AIAA Paper 74-30, Jan. 1974.

[5]Francis, E. C., Carlton, C. H., and Thompson, R. E., "Viscoelastic Rocket Grain Fracture Analysis," *International Journal of Fracture*, Vol. 10, No. 2, 1974, pp. 167–180.

[6]Bencher, C. D., Dauskardt, R. H., and Ritchie, R. O., "Microstructural Damage and Fracture Processes in a Composite Solid-Rocket Propellant," *Journal of Spacecraft and Rockets*, Vol. 32, No. 2, 1995, pp. 328–334.

[7]Schapery, R. A., "Correspondence Principles and a Generalized J-Integral for Large Deformation and Fracture Analysis of Viscoelastic Media," *International Journal of Fracture*, Vol. 25, No. 3, 1984, pp. 195–223.

[8]Schapery, R. A., "Models for Damage Growth and Fracture in Nonlinear Viscoelastic Particulate Composites," *Proceedings of 9th US National Congress for Applied Mechanics*, 1982, pp. 237–245.

[9]Hong, S. D., Fedors, R. F., Schwarzl, F., Moacanin, J., and Landel, R. F., "Analysis of the Tensile Stress–Strain Behavior of Elastomers at Constant Strain Rates. I. Criteria for Separability of the Time and Strain Effects," *Polymer Engineering Science*, Vol. 21, No. 11, 1981, pp. 688–695.

[10]Wong, F. C., and Giasson, L., "Development of a Pseudo Analysis Method and Structural Test Vehicle Fabrication," Defence Research Establishment Valcartier, Rept. TR 2000-152, Val-Belair, QC, Canada, March 2001.

[11]Ramberg, W., and Osgood, W. R., "Description of Stress-Strain Curves by Three Parameters," NACA TN 902, July 1943.

[12]Ferry, J. D., *Viscoelastic Properties of Polymers*, 3rd ed., Wiley, New York, 1980, p. 274.

[13]Hutchinson, J. W., "Singular Behavior at the End of a Tensile Crack Tip in a Hardening Material," *Journal of the Mechanics and Physics of Solids*, Vol. 16, No. 1, 1968, pp. 13–31.

[14]Anderson, T. L., *Fracture Mechanics: Fundamentals and Applications*, 1st ed., CRC Press, Boston, 1991, pp. 143 and 670.

[15]Wong, F. C., and Ait-Kadi, A., "Mechanical Behavior of Particulate Composites: Experiments and Micromechanical Predictions," *Journal of Applied Polymer Science*, Vol. 55, No. 2, 1995, pp. 263–278.

[16]Duncan, E. J. S., and Brousseau, P., "Conversion of Oscillatory Shear Data from Highly Filled Polymers by Direct Numerical Integration," *Rheologica Acta*, Vol. 35, No. 1, 1996, pp. 83–94.

[17]"TableCurve2D—Version 4," SPSS, Inc., Chicago, 1997.

[18]"ANSYS Theory Reference—Release 5.3," ANSYS, Inc., Canonsburg, PA, 1996.

[19]Irons, B. M., "A Frontal Solution Program for Finite Element Analysis," *International Journal for Numerical Methods in Engineering*, Vol. 2, No. 1, 1970, pp. 5–23.

[20]Melosh, R. J., and Bamford, R. M., "Efficient Solution of Load-Deffection Equations," *ASCE Journal of the Structural Division*, Vol. 95, No. ST4, 1969, pp. 661–676.

[21]Simo, J. C., and Taylor, R. L., "Consistent Tangent Operators for Rate-Independent Elastoplasticity," *Computer Methods in Applied Mechanics and Engineering*, Vol. 48, No. 1, 1985, pp. 101–118.

[22]Solecki, J. S., "Fracture Mechanics," ANSYS Rev. 4.4 Tutorial, May 1989.

[23]Francis, E. C., Thompson, R. E., Perkins, S. E., Heerema, S. W., and So, W.-C. T., "Stress Transducer Application Demonstration," U.S. Air Force Philips Lab., Propulsion Directorate, Rept. PL-TR-91-3042, Edwards AFB, CA, March 1992.

[24]Faulkner, G. S., and Tod, D., "Service Life Prediction Methodologies: Aspects of the TTCP KTA-14 UK Programme," *Service Life of Solid Propellant Systems*, CP-586, AGARD, 1996.

[25]Wong, F. C., Firmin, A., and Liu, Y. C., "Verification of the Swanson Nonlinear Thermo-Viscoelastic Model Using Stress Gage Technology," *Service Life of Solid Propellant Systems*, CP-586, AGARD, 1996.

[26]Ho, S. Y., Ide, K., and Macdowell, P., "Instrumented Service Life Program for the Pictor Rocket Motor," *Service Life of Solid Propellant Systems*, CP-586, AGARD, 1996.

[27]Chelner, H., and Buswell, H. J., "Miniature Sensor for Measuring Solid Grain Rocket Motor Case Bond Stress," *Service Life of Solid Propellant Systems*, CP-586, AGARD, 1996.

[28]Erickson, D. E., and Wong, F. C., "Failure Prediction of Solid Rocket Motors on Thermal Cooldown," Defence Research Establishment Valcartier, Rept. DREV TR 2000-025, Val-Belair, QC, Canada, May 2000.

[29]Wong, F. C., and Ait-Kadi, A., "Analysis of Particulate Composite Behavior Based on Non-Linear Elasticity and Modulus Degradation Theory," *Journal of Materials Science*, Vol. 32, No. 19, 1997, pp. 5019–5034.

[30]Hwang, W., Lee, C. S., Park, H. C., and Han, K. S., "Single- and Multi-Stress Level Fatigue Life Predictions of Glass/Epoxy Composites," *Journal of Advanced Materials*, Vol. 26, No. 4, 1995, pp. 3–9.

[31]Little, R. R., "An Investigation of Fracture Characterization for Composite Solid Propellants," Ph.D. Dissertation, Dept. of Mechanical and Aerospace Engineering, Univ. of Alabama, Huntsville, AL, Nov. 1998, pp. 172, 173.

[32]Parks, D. M., "Engineering Methodologies for Assessing Crack Front Constraint," *1991 SEM Spring Conference on Experimental Mechanics*, Society for Experimental Mechanics, Bethel, CT, 1991, pp. 1–8.

[33]Hancock, J. W., Reuter, W. G., and Parks, D. M., "Constraint and Toughness Parameterized by T," American Society for Testing and Materials, Standard TP 1171, 1993, pp. 21–40.

M. P. Nemeth
Associate Editor